Stacking behavior of twin-free type-*B* oriented $CeO_2(111)$ films on hexagonal $Pr_2O_3(0001)/Si(111)$ systems

M. H. Zoellner,* J. Dabrowski, P. Zaumseil, A. Giussani, M. A. Schubert, and G. Lupina
IHP, Im Technologiepark 25, 15236 Frankfurt (Oder), Germany

H. Wilkens, J. Wollschläger, and M. Reichling
Fachbereich Physik, Universität Osnabrück, Barbarastr. 7, 49076 Osnabrück, Germany

M. Bäumer
Institute for Applied and Physical Chemistry, University of Bremen, Leobener Str. NW2, 28359 Bremen, Germany

T. Schroeder
IHP, Im Technologiepark 25, 15236 Frankfurt (Oder), Germany

(Received 9 September 2011; revised manuscript received 27 October 2011; published 3 January 2012)

Tailored CeO_2/Pr_2O_3 thin-film oxide heterostructures are of interest for model catalysis studies by surface science techniques. For this purpose, thin $CeO_2(111)$ films were grown by molecular beam epitaxy on hex-$Pr_2O_3(0001)/Si(111)$ as well as on cub-$Pr_2O_3(111)/Si(111)$ support systems. A comparative, rigorous structure investigation by reflection high-energy electron diffraction transmission electron microscopy and laboratory and synchrotron based x-ray diffraction is reported. It is found that twin-free, exclusively type-B oriented $CeO_2(111)$ films are obtained on both oxide supports. $CeO_2(111)$ films adopt the stacking sequence from the cub-$Pr_2O_3(111)$ buffer, but the transfer of the stacking information is less evident in the case of hex-$Pr_2O_3(0001)$ films. *Ab initio* calculations are applied to understand the unusual stacking behavior of the $CeO_2(111)$ on the hex-$Pr_2O_3(0001)/Si(111)$ system. It is revealed that the type-B stacking configuration is the more favorable configuration by 8 eV/nm^2 due to electronic and crystallographic factors.

DOI: 10.1103/PhysRevB.85.035302 PACS number(s): 68.65.−k, 81.15.Hi

I. INTRODUCTION

Rare-earth oxides (REOs) are of interest in several fields of catalysis, e.g., in oxidative dehydrogenation,[1] oxidative coupling,[2] methane conversion,[3] and three-way catalysis.[4] Especially, the high oxygen mobility and storage capability of REOs, which are the highest for the praseodymium oxide Pr_6O_{11},[5] influence the catalytic activity. The microscopic origin of this behavior arises from the easy exchange in the valence state of Pr^{3+}/Pr^{4+}, where Pr^{3+} is the preferred state under many reaction conditions. Interestingly, the neighboring rare-earth element cerium behaves complementary and prefers the Ce^{4+} valence state in the oxide form. Combining cerium and praseodymium oxides thus enables us to engineer catalysts with tailored reactivity and selectivity by improving the characteristics of the catalyst, e.g., oxygen storage capacity (OSC), oxygen mobility, and thermal stability.[6–9] If such systems are prepared as single-crystalline thin oxide films on plane substrates, they can be used as model catalyst systems. This approach reduces the complexity of investigating three-dimensional (3D) amorphous or polycrystalline materials to surface science studies of two-dimensional (2D) films with specific orientation and defined defect densities. This simplification exhibits the advantage to correlate the catalyst structure with its properties by applying the plethora of surface science tools.[10–12]

For the growth of single-crystalline REO thin films on Si, which might be used as a model catalyst system, a high expertise was developed in the field of microelectronics. Originally, such REOs were investigated for developing high-*k* dielectrics,[13] setting up engineered Si wafers and integrating complex functional oxides on Si.[14–20] In the special case of Pr and Ce oxides, different groups already succeeded to grow epitaxial CeO_2 and Pr_2O_3 thin films on Si(111),[21–25] which could act as appropriate systems for surface science model catalysis. In this paper, we report about combined CeO_2/Pr_2O_3 bilayer systems on Si(111), which are of interest as a model catalyst for CeO_2 with enhanced oxygen storage capacity by charging and discharging the buried Pr_2O_3 layer. Therefore, we have grown $CeO_2(111)$ on top of cub-$Pr_2O_3(111)/Si(111)$ and hex-$Pr_2O_3(0001)/Si(111)$ supports. Before carrying out model catalytic studies, a rigorous structure study of the $CeO_2/Pr_2O_3/Si$ heterostructure must be elaborated and is reported in this paper.

As a main result, it is found that twin-free, exclusively type-B oriented $CeO_2(111)$ films can be grown on cub-$Pr_2O_3(111)/Si(111)$ as well as on hex-$Pr_2O_3(0001)/Si(111)$ support systems. The orientation of the BACBAC... stacking sequence of (111) planes in Si is defined as type-A configuration. Fcc-related layers with (111) orientation, the in-plane orientation of which is rotated by 180° with respect to the Si substrate, exhibit a type-B stacking configuration and an ABCABC... sequence by definition. The growth of type-B $CeO_2(111)/hexPr_2O_3(0001)/Si(111)$ heterostructures is a surprising result because the stacking information from the Si substrate to the $CeO_2(111)$ film should get lost due to the ACACAC... stacking sequence of the hex-$Pr_2O_3(0001)$ film. The so-called stacking twin formation (simultaneous presence of type-A and -B domains) is a known heteroepitaxy problem of (111) oriented cubic lattices on hexagonal lattice surfaces, e.g.,

$In_2O_3(111)/\alpha$-$Al_2O_3(0001)$,[26] γ-$Al_2O_3(111)/\alpha$-$Al_2O_3(0001)$,[27] and epi-Si(111)/hex-$Pr_2O_3(0001)$/Si(111).[28,29] The main objective here is to gain an understanding of the stacking formation mechanism by investigating the twin-free, type-B heteroepitaxial growth of $CeO_2(111)$ on the hex-$Pr_2O_3(0001)$ buffer layer in comparison to the case of cub-$Pr_2O_3(111)$/Si(111) supports. For this reason, we performed an extensive laboratory and synchrotron based structure analysis in combination with crystallographic considerations and *ab initio* theory studies.

II. EXPERIMENTAL DETAILS

On-oriented 4″ boron-doped Si(111) wafers ($\rho = 5$–15 Ωcm) were cleaned using a standard wet etching process with hydrofluoric acid (HF) and an ammonia fluoride (NH_4F) buffer, as explained in detail in a previous publication.[30] After this procedure, the hydrogen-terminated Si wafers were loaded into an ultrahigh vacuum chamber (UHV) with a base pressure of 3×10^{-10} mbar. Annealing the samples at 700 °C for 5 min leads to a high-quality (7 × 7)-Si(111) surface reconstruction. Oxide granulate, evaporated by an electron beam, was used for the molecular beam epitaxy (MBE). The growth of 8-nm single-crystalline hex-$Pr_2O_3(0001)$ film was carried out at 625 °C substrate temperature with a deposition rate of 3 nm/min. For the phase transition to single crystalline, twin-free cub-$Pr_2O_3(111)$, an *ex situ* annealing process was used.[31] CeO_2 was grown afterward on cub-$Pr_2O_3(111)$/Si(111) 22 nm thick and on hex-$Pr_2O_3(0001)$/Si(111) 38 nm thick at the same temperature and deposition rate. During oxide deposition, the chamber pressure raised typically up to 1×10^{-6} mbar without supply of additional oxygen.

An EK 35 reflection high-energy electron diffraction (RHEED) apparatus ($E = 15.8$ keV) from Staib Instruments was used for the *in situ* growth control of the oxide film quality and to monitor the stacking information after each deposition step. Cross-section images of the heterostructures along the Si[−110] direction were recorded, using a Philips CM200 transmission electron microscope (TEM) with a point resolution of 0.27 nm. To characterize the global crystal quality in terms of layer orientation, x-ray diffraction (XRD) was carried out *ex situ* with a DMAX 1500 and a SmartLab from Rigaku [Cu K_α radiation ($\lambda = 0.154$ nm)]. In addition, synchrotron radiation-grazing incidence x-ray diffraction (SR-GIXRD) measurements at the beam line W1 of the Hamburger Synchrotronstrahlungslabor (HASYLAB) were performed ($E = 10.5$ keV) to achieve a structure analysis of the $CeO_2(111)$/hex-$Pr_2O_3(0001)$/Si(111) heterostructure with high resolution and sensitivity.

Ab initio calculations were carried out with the parallelized pseudopotential plane-wave code QUANTUM ESPRESSO.[32] Exchange and correlation energies were expressed in the local density approximation (LDA) form, as parametrized by Perdew and Zunger.[33] Oxygen, silicon, and hydrogen atoms were described with pseudopotentials from ESPRESSO distribution (ultrasoft pseudopotentials were used for oxygen). For praseodymium and cerium atoms, custom pseudopotentials were created. The $n = 5$ shell electrons were treated as semicore electrons.[34] In order to circumvent the LDA problem with the open f shell, the $4f$ shell was frozen in the core. Consequently, the lanthanide atoms Ln with valence 3 and 4 (Ln^{3+} and Ln^{4+}, where Ln = Ce, Pr) were represented by separate pseudopotentials, meaning that in the calculation they were treated as separate species: the number of f electrons was fixed and no conversion between the Ln^{3+} and Ln^{4+} "species" was possible during the self-consistent run. All four Ln pseudopotentials included the $5p$ shell as semicore electrons. The pseudopotentials were verified to be free of ghost states. They reproduced the lattice parameters of the corresponding bulk oxide with an accuracy better than 1%, which is typical for this kind of calculation. Also, the computed bulk moduli were in a satisfactory agreement with the experimental data.[35] For the interface calculations, the Brillouin zone was sampled with eight surface special k points equivalent to the $(\frac{1}{4}, \frac{1}{4}, 0)$ point of the 5×3 primitive rectangular surface cell with dimensions 1.945×2.021 nm^2, corresponding to volume-relaxed hexagonal Pr_2O_3 bulk. The energy cutoff for plane waves was set to 40 Ry.

III. RESULTS AND DISCUSSION

A. RHEED

A RHEED study was applied to *in situ* monitor the structural properties of the CeO_2/cub-Pr_2O_3/Si(111) [Figs. 1(a) and 1(b)] and CeO_2/hex-Pr_2O_3/Si(111) [Figs. 1(c) and 1(d)] heterostructures [electron beam oriented along the stacking sensitive ⟨−110⟩ azimuth of Si(111)]. The RHEED images [Figs. 1(a)–1(d)] show spotty patterns due to the onset of 3D growth. The latter fact allows deducing first insights regarding the vertical oxide orientation, as described in detail below.

As illustrated by the dashed lines, a twin-free, type-B oriented cub-$Pr_2O_3(111)$ surface diffraction pattern is visible in the RHEED image, Fig. 1(a). This result is in good

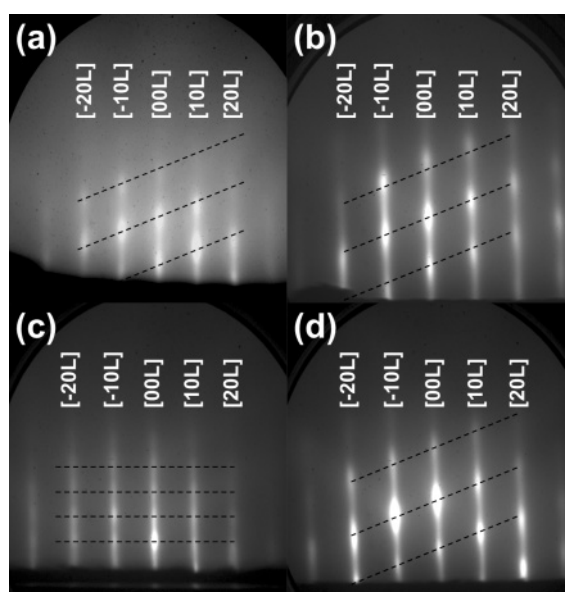

FIG. 1. RHEED images along the Si⟨−110⟩ azimuth of a (a) type-B oriented cub-$Pr_2O_3(111)$ surface on Si(111); (b) type-B oriented $CeO_2(111)$ surface on cub-$Pr_2O_3(111)$/Si(111) support; (c) hex-$Pr_2O_3(0001)$ surface on Si(111); and (d) type-B oriented $CeO_2(111)$ surface on hex-$Pr_2O_3(0001)$/Si(111) support.

agreement with the expected theoretical Bragg peak distribution of cub-Pr_2O_3(111)/Si(111) systems.[36] After CeO_2 deposition, no substantial change in the intensity distribution of the RHEED pattern is observed. The RHEED image, Fig. 1(b), shows again the typical surface diffraction pattern of a twin-free, type-B oriented CeO_2(111) film. In consequence, the CeO_2(111) film adopted the type-B stacking information from the cub-Pr_2O_3(111)/Si(111) system. This behavior is expected for oxide/oxide epitaxy and was previously reported for similar material systems (e.g., cub-Y_2O_3/cub-Pr_2O_3).[37] In accord with the RHEED study, the epitaxial relationship of the heterostructure is thus given by CeO_2(111); ⟨1-10⟩||cub-Pr_2O_3(111); ⟨1-10⟩||Si(111); ⟨−110⟩.

In Fig. 1(c), the RHEED diffraction pattern of the hex-Pr_2O_3(0001) surface is shown. This is in agreement with the expected, theoretical Bragg peak distribution of a (0001) oriented hex-Pr_2O_3 film.[30] Surprisingly, CeO_2 deposition results in a RHEED image Fig. 1(d), which is identical with Fig. 1(b) and characteristic of a twin-free, exclusively type-B oriented CeO_2(111) layer. In other words, the RHEED study indicates a CeO_2(111)⟨1-10⟩||hex-Pr_2O_3(0001); ⟨11-20⟩||Si(111);⟨−110⟩ epitaxial relationship.

In conclusion, one can say that no stacking twins are detectable with RHEED in the CeO_2(111) film, neither on cub-Pr_2O_3(111) nor on hex-Pr_2O_3(0001). For a further corroboration of the result, we performed an *ex situ* TEM and XRD structure analysis with better resolution and higher sensitivity.

B. TEM

Figures 2(a) and 2(b) show high-resolution transmission electron microscope (HRTEM) cross-section images from CeO_2(111)/cub-Pr_2O_3(111)/Si(111) and CeO_2(111)/hex-Pr_2O_3(0001)/Si(111), respectively. Along the ⟨−110⟩ direction, the BACBAC... stacking sequence in the [111] direction of the Si(111) substrate is clearly visible. The stacking orientation is indicated by an arrow pointing to the [11-1] direction. The approximate positions of the interfaces (IFs) are denoted by arrows at the pictures' sides. As explained in previous studies,[28,37,38] post-deposition oxidation during the phase transition from hexagonal to cubic Pr_2O_3 results in an IF layer [bright contrast in Fig. 2(a)] between the oxide and the Si(111) substrate. The annealed cub-Pr_2O_3(111) layer exhibits an ABCABC...stacking sequence, due to a 180° rotation around the [111] surface normal. The indicated [11-1] direction reveals the so-called type-B orientation of the cub-Pr_2O_3(111) layer. The (11-1) planes were identified by their 71° tilt with respect to the (111) planes. The CeO_2(111)/cub-Pr_2O_3(111) IF is difficult to identify due to the similar projected potentials and crystal structures. Thus, its position is identified by IF defects between the oxides. Figure 2(a) highlights the presence of an edge dislocation at the IF, namely, an additional (11-1) plane is present in the smaller CeO_2 lattice with respect to the bigger Pr_2O_3 lattice. The in-plane lattice mismatch of the CeO_2(111) and cub-Pr_2O_3(111) planes, which will be discussed in detail later, is partially compensated in this way. The [11-1] directions of the CeO_2(111) and cub-Pr_2O_3(111) layers are parallel to each other, representing the common type-B stacking orientation, which the CeO_2(111) layer adopted from the cub-Pr_2O_3(111)/Si(111) support.

Figure 2(b) of the CeO_2(111)/hex-Pr_2O_3(0001)/Si(111) heterostructure also reveals an amorphous interfacial layer between the as-grown hex-Pr_2O_3(0001) and the Si(111) substrate. This is a surprising result because as-deposited hex-Pr_2O_3(0001) films were reported to grow without an IF layer on Si(111) and even the atomic structure for monolayer films was solved by GI-XRD studies.[25,39,40] Therefore, we suggest that, during the deposition of CeO_2, excess oxygen diffuses to the hex-Pr_2O_3(0001)/Si(111) IF and causes a post-deposition oxidation. In contrast, the CeO_2(111)/hex-Pr_2O_3(0001) IF is atomically sharp, and no crystal defects were identified in our TEM analysis. Therefore, we expect a smaller in-plane

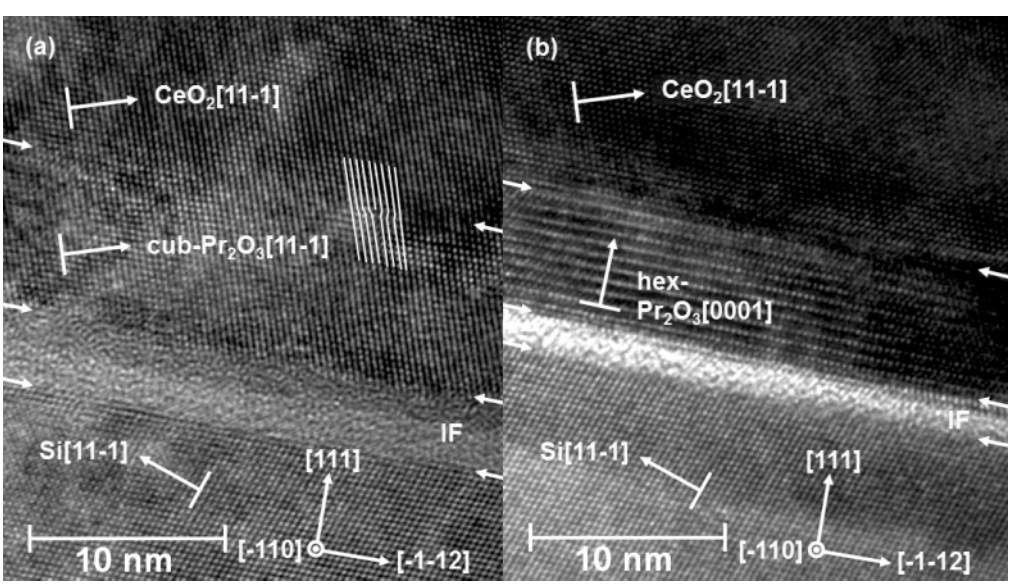

FIG. 2. HRTEM cross-section images along the Si[−110] direction of (a) CeO_2(111)/cub-Pr_2O_3(111)/Si(111) and (b) CeO_2(111)/hex-Pr_2O_3(0001)/Si(111).

lattice mismatch from the $CeO_2(111)$ film relative to the hex-$Pr_2O_3(0001)$/Si(111) support. Furthermore, we can again identify the [11-1] direction of the $CeO_2(111)$ layer, which is also rotated by 180° with respect to Si[111], confirming with lattice resolution the type-B stacking orientation.

In consequence, RHEED as well as TEM indicates the growth of purely type-B oriented $CeO_2(111)$ films on cub-$Pr_2O_3(111)$/Si(111) and hex-$Pr_2O_3(0001)$/Si(111) supports. However, we have to consider that cross-section TEM images only reveal very local and no global information. Therefore, laboratory and synchrotron based XRD studies are applied to complement the structure analysis of the oxide heterostructures on a global scale.

C. XRD

To explain the direction of the Bragg peaks in the reciprocal space with respect to the Si(111) surface, we have to transform the bulk $[hkl]$ to the surface $[HKL]$ indices and vice versa. Under the assumption that Si and CeO_2 exhibit the same lattice constant, the transformation can be carried out by these operations:

$$\begin{bmatrix} h \\ k \\ l \end{bmatrix}_{\text{bulk}}^{\text{CeO}_2} = \frac{1}{6}\begin{bmatrix} -4 & 4 & 6 \\ -4 & -8 & 6 \\ 8 & 4 & 6 \end{bmatrix}\begin{bmatrix} H \\ K \\ L \end{bmatrix}_{\text{surf}}^{\text{Si}},$$
$$\begin{bmatrix} H \\ K \\ L \end{bmatrix}_{\text{surf}}^{\text{CeO}_2} = \frac{1}{6}\begin{bmatrix} -3 & 0 & 3 \\ 3 & -3 & 0 \\ 2 & 2 & 2 \end{bmatrix}\begin{bmatrix} h \\ k \\ l \end{bmatrix}_{\text{bulk}}^{\text{Si}}. \quad (1)$$

Accordingly, a schematic drawing of reciprocal space is shown in Fig. 3 for a reciprocal lattice plane spanned by the [111] surface normal and the [11-2] azimuth. To denote the bulk $[hkl]$ and surface $[HKL]$ indices, they are labeled by bulk and surf, respectively. The CeO_2 indices already include the type-B orientation. On top of the sketch, one can see the surface nomenclature to denote the different crystal truncation rods. The Bragg reflections, corresponding to a type-B orientation, are labeled by open circles. Using the $[10L]_{\text{surf}}$ rod as an example, the potential Bragg peaks of type-A oxide twins are also indicated by open squares. Their L positions match to the open circles of the $[-10L]_{\text{surf}}$ rod due to the 180° rotation symmetry around the [111] direction of stacking twins. Furthermore, the schematic reciprocal lattice plane discussed in Fig. 3 is identical with the one recorded in our RHEED study (Fig. 1). The dashed lines in Figs. 1(a), 1(b), and 1(d) are reproduced in Fig. 3 and illustrate the common diffraction peak distribution of (111) oriented, fcc-related oxide epilayers.

We start the qualitative XRD structure analysis with wide-angle specular Θ-2Θ scans from 20° to 105° presented in Fig. 4(a). In surface coordinates, this corresponds to a scan along the $[00L]_{\text{surf}}$ rod. These scans allow us to corroborate the vertical epitaxial relationship of the oxide heterostructures on Si(111). The sharp and most intense double peaks can be assigned to $K_{\alpha 1}$ and $K_{\alpha 2}$ of the Si(111) reflection and its higher orders (222) and (333). The Bragg peaks of the hex-$Pr_2O_3(0001)$ layer [Fig. 4(a), lower curve] are designated as $(000n)$ reflections ($n = 2$–6). The (222), (444), and (666) reflections of the cub-$Pr_2O_3(111)$ layer [Fig. 4(a), upper curve]

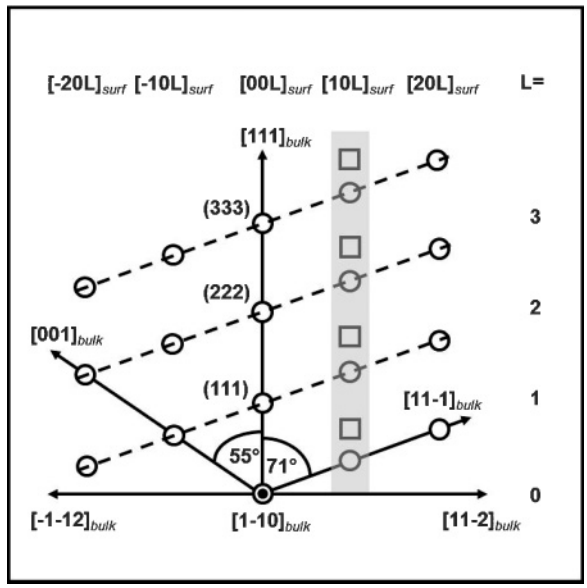

FIG. 3. Schematic drawing of reciprocal space in surface coordinates along the [1-10] direction of fcc-related, (111) oriented surfaces. The open circles are defined to the reflections of a type-B oriented film and in the $[10L]_{\text{surf}}$ rod potential reflections of type-A oriented domains are assigned by open squares.

are also indicated.[25,30] The labeled $CeO_2(111)$, (222), and (333) reflections are identified to be located close to the positions of the respective Si(nnn) ($n = 1, 2, 3$) Bragg peaks.

In the following, the strain status of the CeO_2 film is analyzed in a quantitative way. Therefore, we first enlarged the section around the Si(222) reflection from 52.5° to 67.5° [Fig. 4(b)] because the kinematically forbidden Si(222) Bragg peak exhibits the lowest intensity. The $CeO_2(222)$ reflection at $2\Theta = 59.24°$ (lattice spacing $d_{(222)} = 1.558$ Å) on the hex-$Pr_2O_3(0001)$ support [Fig. 4(b), lower curve] is close to the theoretical bulk value ($2\Theta = 59.09°$; $d_{(222)} = 1.562$ Å). In consequence, $CeO_2(111)$ films grow apparently fully relaxed on hex-$Pr_2O_3(0001)$. In contrast, the lateral lattice mismatch between $CeO_2(111)$ and cub-$Pr_2O_3(111)$ should be much bigger so that a strong in-plane tensile strained $CeO_2(111)$ film is expected, causing compression in vertical direction. Indeed, we observe a shift to higher angles of the $CeO_2(222)$ reflection ($2\Theta = 59.84°$; $d_{(222)} = 1.544$ Å) on the cub-$Pr_2O_3(111)$ buffer layer [Fig. 4(b), upper curve].

The tetragonal distortion of the oxide lattice can be determined by the so-called $\cos^2\chi_{(hkl)}$ method described in Ref. 41, where Bragg reflections of different inclinations $\chi_{(hkl)}$ are analyzed. $\chi_{(hkl)}$ is given by the angle between the surface normal of the (111) and the measured (hkl) net plane. Under the assumption that the distortion is small compared to the cubic lattice constant a, one can calculate from the measured Bragg peak position a theoretical cubic lattice constant $a_{(hkl)}$. Thus, plotting $a_{(hkl)}$ versus $\cos^2\chi_{(hkl)}$ allows one to deduce the in-plane lattice constant a_0 at $\cos^2\chi_{(hkl)} = 0$, which is equivalent to a 90° sample tilt. For a direct comparison with the in-plane lattice constant of hex-Pr_2O_3, Figs. 4(c) and 4(d) show similar plots with $a_{(hkl)}/\sqrt{2}$ for $CeO_2(111)$/cub-$Pr_2O_3(111)$/Si(111) and $CeO_2(111)$/hex-$Pr_2O_3(0001)$/Si(111), respectively. Therefore, the $\chi_{(11-1)} =$

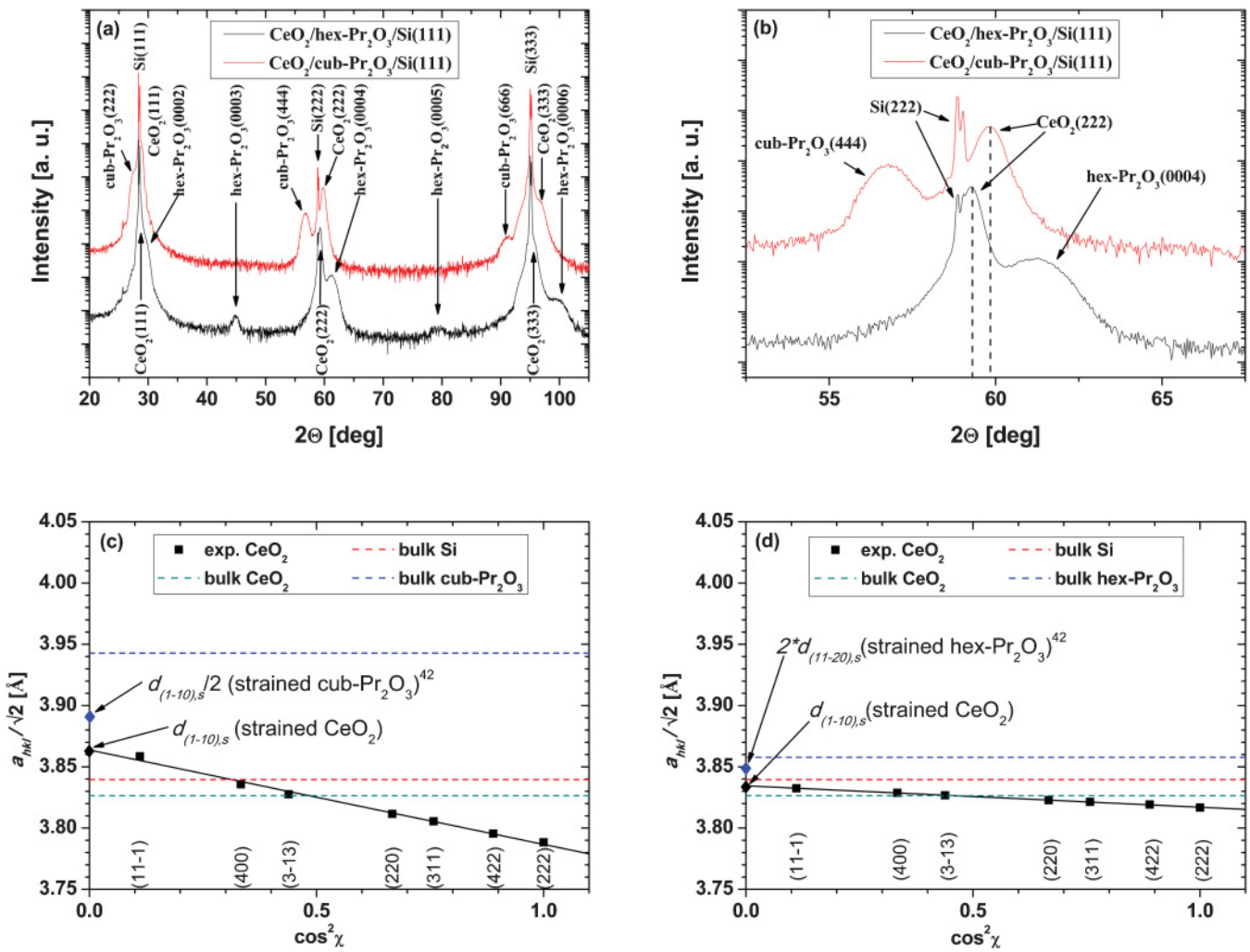

FIG. 4. (Color online) XRD specular Θ-2Θ measurements of $CeO_2(111)$/hex-$Pr_2O_3(0001)$/Si(111) (lower curve) and $CeO_2(111)$/cub-$Pr_2O_3(111)$/Si(111) (upper curve) (a) with a wide angular scan from 20° to 105° and (b) with an enlarged section from 52.5° to 67.5°. Strain measurement using a $\cos^2\chi_{(hkl)}$ plot of the $CeO_2(111)$ film on (c) cub-$Pr_2O_3(111)$/Si(111) and (d) hex-$Pr_2O_3(0001)$/Si(111) support.

70.5°, $\chi_{(400)} = 54.7°$, $\chi_{(3-13)} = 48.5°$, $\chi_{(220)} = 35.3°$, $\chi_{(311)} = 29.5°$, $\chi_{(422)} = 19.5°$, and $\chi_{(222)} = 0°$ angles were used for the corresponding reflections. From the linear regression [Fig. 4(c)], a strained in-plane lattice spacing of $d_{(1-10),s} = 3.864$ Å can be determined for the $CeO_2(111)$ film on cub-$Pr_2O_3(111)$/Si(111). In comparison to the bulk in-plane lattice spacing $d_{(1-10),b} = 3.826$ Å, a lateral tensile strain of +0.78% is resulting. In contrast, the tensile strain in the $CeO_2(111)$ film on hex-$Pr_2O_3(0001)$/Si(111) amounts to only +0.21% [Fig. 4(d)], resulting from the extrapolated in-plane lattice spacing $d_{(1-10),s} = 3.834$ Å. The coefficient of determination from the linear regressions amount to $R^2 = 0.992$ and $R^2 = 0.999$ for Figs. 4(c) and 4(d), respectively. We assume that the bigger in-plane tensile strain from $CeO_2(111)$ on cub-$Pr_2O_3(111)$/Si(111) compared to $CeO_2(111)$ on hex-$Pr_2O_3(0001)$/Si(111) is caused by the bigger lattice mismatch. Therefore, we have previously to consider the strained in-plane lattice spacings of hex-$Pr_2O_3(0001)$ ($2d_{(11-20),s} = 3.849$ Å) and cub-$Pr_2O_3(111)$ ($d_{(1-10),s}/2 = 3.890$ Å) on Si(111), which were determined to be typical results in a thickness range from 4–13 nm.[42] These values are indicated in Figs. 4(c) and 4(d). Note that cub-$Pr_2O_3(111)$ has a four times bigger in-plane surface unit cell than Si(111). From these results, a lattice mismatch of bulk $CeO_2(111)$ ($d_{(1-10),b} = 3.826$ Å) to strained hex-$Pr_2O_3(0001)$ buffer layers (−0.60%) and to cub-Pr_2O_3 buffer layers (−1.65%) arises. As expected, the cub-$Pr_2O_3(111)$/Si(111) support exhibits the bigger lattice mismatch, causing the bigger strain in the $CeO_2(111)$ film.

To analyze now the stacking characteristics, we need in-plane as well as off-plane information. Figures 5(a) and 5(b) show Φ scans around the Si[111] axis of the $CeO_2\{-111\}$ and Si$\{-111\}$ reflections from $CeO_2(111)$/cub-$Pr_2O_3(111)$/Si(111) ($2\Theta = 28.4°$) and $CeO_2(111)$/hex-$Pr_2O_3(0001)$/Si(111) ($2\Theta = 28.5°$) heterostructures. Due to the high crystal quality of the silicon wafers, the sharp peaks can be easily assigned to the Si$\{-111\}$ reflections. These are separated by 120° around the [111] surface normal, due to the threefold off-plane symmetry around the cubic Si⟨111⟩ space diagonal (Fd-$3m$). Accordingly, the broader $CeO_2\{-111\}$ peaks are rotated by 180° in respect to the Si$\{-111\}$ peaks in Figs. 5(a) and 5(b). This experimental result is a clear proof of the type-B orientation of the $CeO_2(111)$ film,

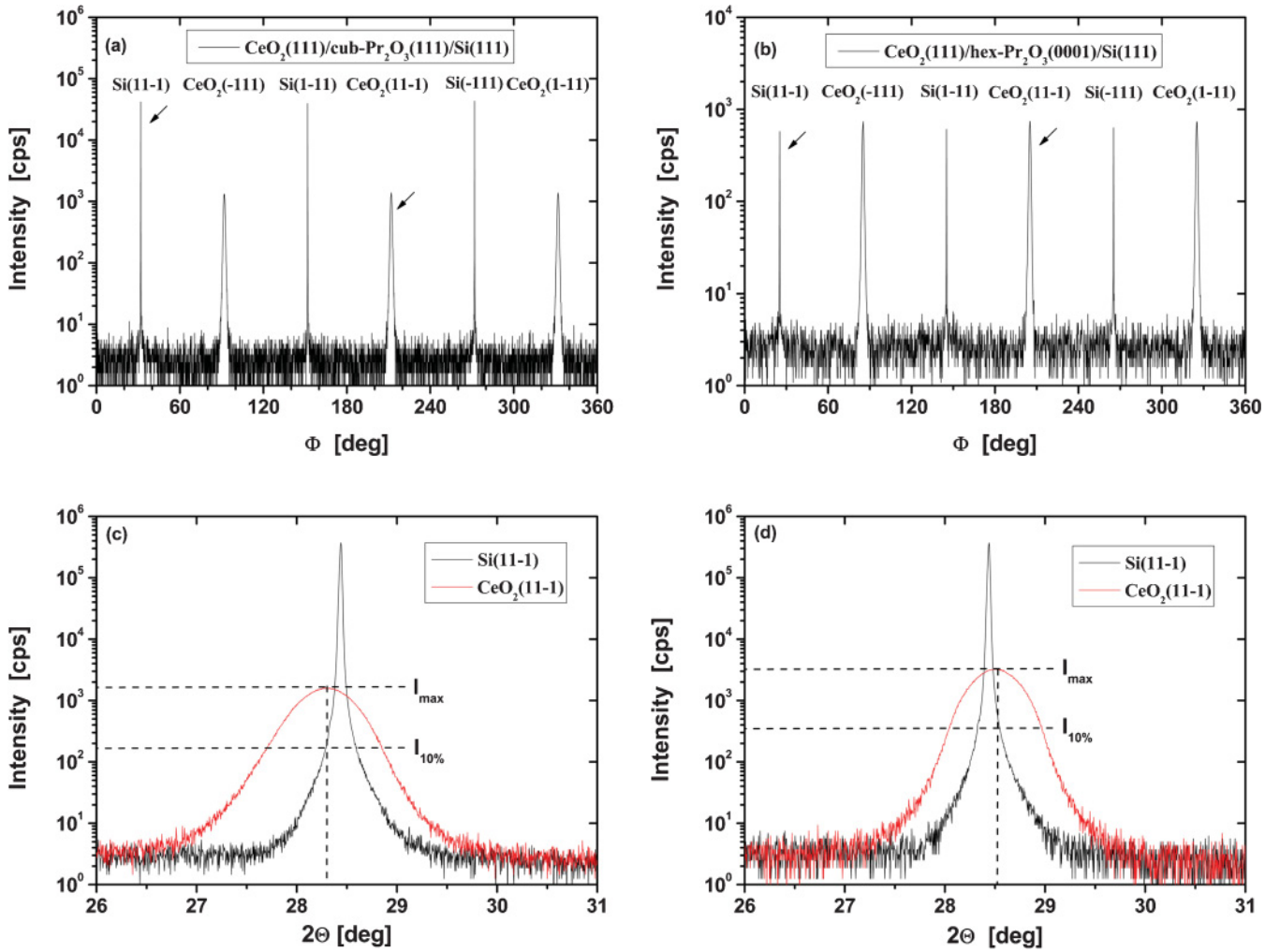

FIG. 5. (Color online) Twin analysis via Φ scan around the Si[111] axis (a) at $2\Theta = 28.4^\circ$ of CeO_2(111)/cub-Pr_2O_3(111)/Si(111) (b) at $2\Theta = 28.5^\circ$ of CeO_2(111)/hex-Pr_2O_3(0001)/Si(111). HRXRD Θ-2Θ scans on the Si(11-1) Bragg peak (the broad peak) and the CeO_2(11-1) Bragg peak (the sharp peak) with Φ rotated about 180° of (c) CeO_2(111)/cub-Pr_2O_3(111)/Si(111) and (d) CeO_2(111)/hex-Pr_2O_3(0001)/Si(111).

which confirms the $CeO_2\langle$1-10$\rangle$||cub-$Pr_2O_3\langle$1-10$\rangle$||Si$\langle-110\rangle$ and $CeO_2\langle$1-10$\rangle$||hex-$Pr_2O_3\langle$11-20$\rangle$||Si$\langle-110\rangle$ lateral epitaxial relationships.

The absence of stacking twins or rather type-A domains had to be verified by HRXRD measurements. Therefore, the Si(11-1) and CeO_2(11-1) reflections [labeled by arrows in Figs. 5(a) and 5(b)] are compared to each other in Fig. 5(c) [CeO_2(111)/cub-Pr_2O_3(111)/Si(111)] and Fig. 5(d) [CeO_2(111)/hex-Pr_2O_3(0001)/Si(111)] by Θ-2Θ scans. The respective Si(11-1) (sharp peak) and CeO_2(11-1) (broad peak) reflections are related to each other by a 180° in-plane rotation. Referring to the maximum intensity I_{max} of the CeO_2(11-1) peak, we conclude that no type-A CeO_2 Bragg peak is present at the position of the Si(11-1) peak with an intensity of more than 1/10 of the type-B CeO_2 Bragg peak intensity [$I_{10\%}$ criteria in Figs. 4(c) and 4(d)]. In other words, as no shoulder is visible in the Si(11-1) Bragg peak on the position of the CeO_2(11-1) reflection, we can estimate from the HRXRD study that less than 10% of the CeO_2 film might exhibit a type-A stacking on the cub-Pr_2O_3(111)/Si(111) as well as on the hex-Pr_2O_3(0001)/Si(111) support. To give a more precise estimate of the type-A/B ratio in the CeO_2(111) film on the hex-Pr_2O_3(0001) buffer layer, high-sensitivity SR-GIXRD studies are discussed in the following.

D. SR-GIXRD

For CeO_2(111)/hex-Pr_2O_3(0001)/Si(111) heterostructures, we performed SR-GIXRD scans along the $[10L]_{surf}$ rod [Fig. 6(a)] and $[01L]_{surf}$ rod [Fig. 6(b)]. Aside from Si(111) surface coordinates, important Bragg peaks are labeled in bulk coordinates. Concerning the $[10L]_{surf}$ rod [Fig. 6(a)], the (11-1) and (220) peak positions of the type-A Si(111) are located at $L = 1/3$ and 4/3 r.l.u., respectively. Due to the 180° in-plane rotation of the type-B oriented CeO_2(111) film, its (002) and (113) reflections are located at $L = 0.670$ and 1.675 r.l.u., respectively. However, the potential XRD signals of a type-A stacking CeO_2 domain would overlap again with the peak positions of the more intense type-A Si substrate. In addition, it is noted that the Pr_2O_3 reflections (10-1n) along the $[10L]_{surf}$ rod appear at $L = 0.517n$ r.l.u. ($n = 1, 2, 3,...$)

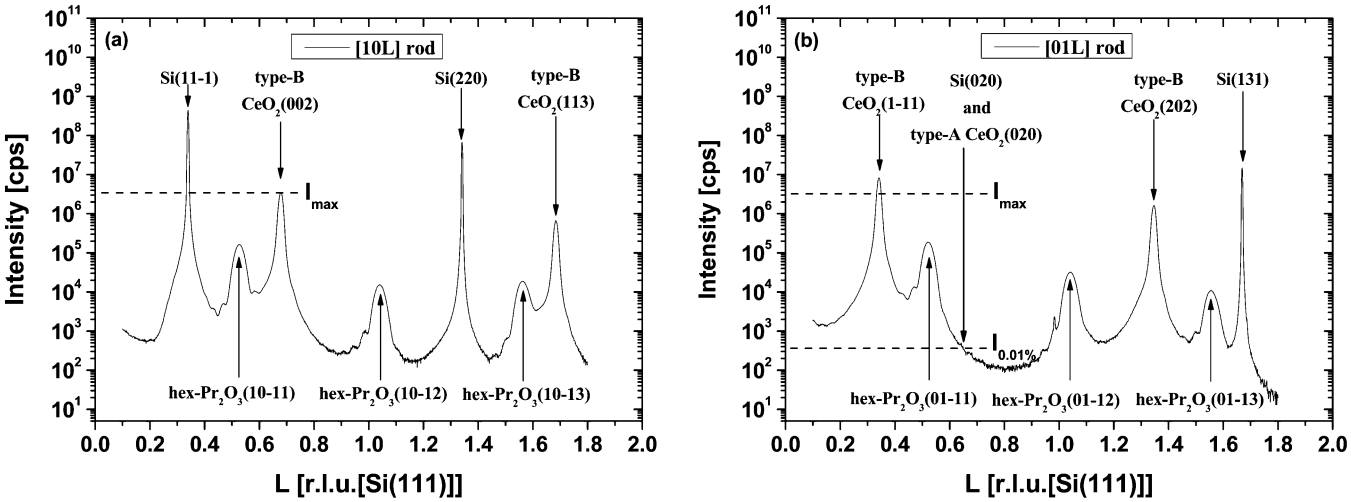

FIG. 6. SR-GIXRD of $CeO_2(111)$/hex-$Pr_2O_3(0001)$/Si(111) along the (a) $[10L]_{surf}$ rod and (b) $[01L]_{surf}$ rod.

because the (0001) lattice spacing of hex-Pr_2O_3 is about twice as big as the Si(111) net plane distance.

To achieve a more precise stacking twin analysis, the $[01L]_{surf}$ rod is studied [Fig. 6(b)]. Again, the hex-Pr_2O_3 reflections (01-1n) are located at $L = 0.517n$ r.l.u. ($n = 1$, 2, 3,...). On the $[01L]_{surf}$ rod, we can identify the CeO_2(1-11) and (202) reflections at $L = 0.335$ and 1.340 r.l.u. of type-B $CeO_2(111)$ film. Here, the type-A Si(131) peak is visible at 5/3 r.l.u. and the kinematically forbidden Si(020) reflection is located at $L = 2/3$ r.l.u. As the latter reflection is forbidden, this exhibits the chance to detect the potential presence of type-A stacking CeO_2 domains with high precision at this position. The fact that also the allowed $CeO_2(020)$ reflection is not visible with 0.01% intensity $I_{0.01\%}$ of the $CeO_2(002)$ maximum intensity I_{max} corroborates finally the previous discussions that no type-A oriented $CeO_2(111)$ domains can be found in the type-B oriented $CeO_2(111)$ layer on the hex-$Pr_2O_3(0001)$/Si(111) support within the detection limit, even with such a potent investigation method as SR-GIXRD.

E. *Ab initio* calculations

Next, we discuss the physical mechanisms responsible for the observed growth of twin-free, type-B oriented $CeO_2(111)$ on hex-$Pr_2O_3(0001)$/Si(111). As outlined in the Introduction, it is by far not self-evident that the type-B interface is strongly preferred. In order to elucidate the reasons for this preference, we performed *ab initio* calculations for interfaces of type-B [Fig. 7(a)] and type-A [Fig. 7(b)]. The results are in agreement with the experimental data and reveal that the interface of type-B is strongly favored, with the energy difference amounting to 2.2 eV per surface cell, i.e., to 8 eV/nm^2. In brief, we find that this effect is attributed to an interplay of electronic and crystallographic factors. First, the valence mismatch at the CeO_2/Pr_2O_3 interface layer leads to conversion of Pr^{3+} to Pr^{4+}, i.e., to the reduction of the number of f electrons on Pr from two to one. Second, the interface of type-B corresponds to a topologically smooth transition from CeO_2 to Pr_2O_3, while the interface of type-A leads to the appearance of a topological stacking fault. The details are explained below.

For completeness, the interface between the oxides and the interface to Si were included in the calculation. For the latter, the configuration determined by Jeutter *et al.*[40] was used. This interface contains an additional layer of oxygen bonded to Si needed to compensate the bonding-type mismatch between Pr_2O_3 and Si and to bind all electrons donated by Pr^{3+}. Similar mismatch appears at the interface between CeO_2 and hex-Pr_2O_3, where it is compensated by electrons from Pr. The interfacial Pr atoms lose one f electron each and transform from Pr^{3+} (light blue) to Pr^{4+} (dark blue). This produces a monatomic PrO_2 interface layer and conserves the semiconducting character of the CeO_2/Pr_2O_3 interface. As a result, all Ln atoms (Ce^{4+}, Pr^{4+}) at the chemical interface have the same valence and prefer the same arrangement of oxygen neighbors, namely, that of cubic LnO_2, the fluorite structure.

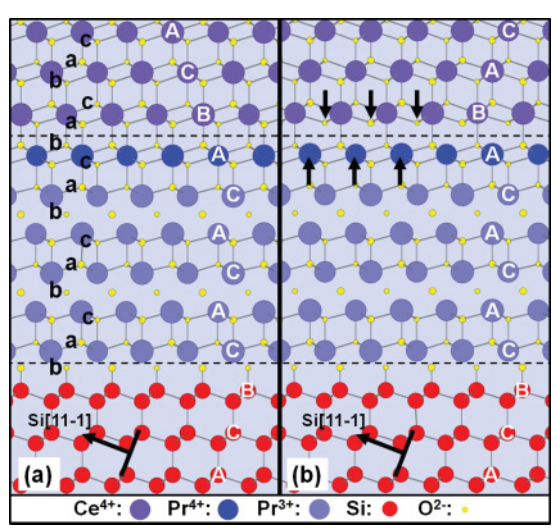

FIG. 7. (Color online) Stacking configuration models along the Si[−110] direction of (a) type-B $CeO_2(111)$/hex-$Pr_2O_3(0001)$/Si(111) and (b) type-A $CeO_2(111)$/hex-$Pr_2O_3(0001)$/Si(111).

The interface of type-B [Fig. 7(a)] provides this arrangement in a natural way, resulting from the stacking of atomic planes in both materials. This becomes apparent by looking at the sublattice of the hex-Pr_2O_3 layer. Indeed, the praseodymium sublattice exhibits the ACACAC... stacking sequence, while the stacking of the oxygen sublattice follows the bacbac... pattern, as pointed out by Eyring and his notation.[43] After the conversion to PrO_2 at the interface, the Pr_2O_3 film becomes a topological continuation of the CeO_2 film above it. Since the oxygen sublattice of CeO_2 exhibits the same bacbac... stacking sequence as in Pr_2O_3, the only structural adjustment that takes place at the interface is some relatively minor shift of interfacial oxygen atoms of the praseodymium oxide. These atoms move toward the bulk Pr_2O_3 in response to the increased positive charge of interfacial Pr atoms. The C-terminated geometry, in which all Pr^{4+} atoms of layer A in Fig. 7 are substituted by Ce^{4+} atoms, is likely to be energetically comparable to the A-terminated geometry assumed in Fig. 7. Namely, this substitution conserves the charge of metal atoms, and also the distance between B and A layers in CeO_2 is close to the distance between the B and A layers at the chemical interface, as well as to the distance between the interfacial A layer and the C next layer in Pr_2O_3. This topological coherence between hex-Pr_2O_3(111) and CeO_2(111) provides also a natural means to compensate any local thickness variations on the monatomic scale.

In other words, when the interface is of type-A [Fig. 7(b)], there is a topological (111) stacking fault between PrO_2 and CeO_2. The interface oxygen atoms of the CeO_2 film are out of registry for the Pr^{4+}, causing a reduced coordination for the Pr^{4+} and for the interfacial oxygen atoms [indicated in Fig. 7(b) by arrows]. We, thus, conclude that the observation of twin-free, exclusively type-B growth of CeO_2(111)/hex-Pr_2O_3(0001)/Si(111) heterostructures is attributed to the formation of a PrO_2 interface layer in response to valence mismatch between a lanthanide dioxide and a lanthanide sesquioxide, to similar stacking of oxygen atomic planes in hexagonal sesquioxide and in the cubic dioxide, and to purely geometrical differences in the stacking of atomic planes for interfaces of types A and B.

IV. CONCLUSION AND OUTLOOK

In summary, we have grown epitaxial CeO_2/cub-Pr_2O_3/Si(111) and CeO_2/hex-Pr_2O_3/Si(111) heterostructures with MBE monitored by RHEED, which showed the following vertical and azimuthal epitaxial relationships for the respective heterostructures:

$CeO_2(111);\langle 1\text{-}10\rangle \| \text{cub-}Pr_2O_3(111);\langle 1\text{-}10\rangle \| \text{Si}(111);\langle -110\rangle$,
$CeO_2(111)\langle 1\text{-}10\rangle || \text{hex-}Pr_2O_3(0001);\ \langle 11\text{-}20\rangle || \text{Si}(111);\langle -110\rangle$.

However, this result is very surprising because, on the ACACAC... stacking sequence of the hex-Pr_2O_3(0001)/Si(111) support, the stacking information for an ABCABC... pattern of CeO_2(111) planes should be lost. So we had to corroborate the RHEED results with further measurements. HRTEM confirmed the epitaxial relationships with atomic resolution. Additionally, an edge dislocation was highlighted in the CeO_2(111) film on cub-Pr_2O_3(111)/Si(111), which is based upon in-plane lattice mismatch and the corresponding lateral tensile strain. The strain status could be verified by XRD, approximating the in-plane lattice spacings in a $\cos^2\chi_{(hkl)}$ plot for CeO_2(111) on cub-Pr_2O_3(111)/Si(111) (+0.78%) and on hex-Pr_2O_3(0001)/Si(111) (+0.21%). The vertical and lateral epitaxial relationships were confirmed on a global scale by Θ-2Θ and Φ scans, respectively. The amount of type-A domains in the type-B CeO_2(111) layer was determined to be much less than 10% by laboratory HRXRD measurements. An SR-GIXRD study of the $[10L]_{\text{surf}}$ rod and the $[01L]_{\text{surf}}$ rod finally revealed that even less than 0.01% type-A CeO_2 domains can be detected in the CeO_2(111) film on the hex-Pr_2O_3(0001)/Si(111) support.

Theoretical *ab initio* calculations demonstrated that this type-B stacking configuration of CeO_2(111) net planes is caused by geometrical differences. First, an interfacial PrO_2 layer is formed to conserve the semiconducting characteristics. Due to this dioxide formation, the type-B interface provides a topological continuation of the bacbac... stacking sequence of the oxygen sublattice. In contrast, a type-A interface would form a (111) stacking fault, reducing the coordination of the interfacial praseodymium and oxygen atoms. Thus, the type-B stacking configuration is preferred by 2.2 eV per surface cell, i.e., by 8 eV/nm^2, in comparison to the type-A interface.

In view of future model catalytic application, experiments concerning the charging and discharging of the Pr_2O_3 buffer layer with oxygen will be performed. Furthermore, the deposition of mixed $Ce_{1-x}Pr_xO_{2-\delta}(x = 0 - 1)$ exhibits the opportunity to tune the OSC as well as the oxygen mobility. Adsorption of different gases and the resulting influence to electrical characteristics in dependence of the stoichiometry will be of interest.

ACKNOWLEDGMENTS

Portions of this research were carried out at the light source W1 at DESY, which is a member of the Helmholtz Association (HGF). We would like to thank W. Caliebe for assistance. *Ab initio* calculations were performed on the JUROPA supercomputer in Jülich within the Neumann Institute for Computing (NIC) Grant No. hfo06. Furthermore, we are grateful to the "Deutsche Forschungsgemeinschaft" (DFG) for financial support.

*zoellner@ihp-microelectronics.com

[1] O. V. Buyevskaya, D. Wolf, and M. Baerns, Catal. Today **62**, 91 (2000).
[2] K. Asami, K. Kusakabe, N. Ashi, and Y. Ohtsuka, Appl. Catal., A **156**, 43 (1997).
[3] K. Otsuka, Y. Wang, E. Sunada, and I. Yamanaka, J. Catal. **175**, 152 (1998).
[4] J. Kaspar, P. Fornasiero, and M. Graziani, Catal. Today **50**, 285 (1999).
[5] G. V. Antoshin, K. M. Minachev, and R. V. Dmitriev, Russ. Chem. Bull. **16**, 1793 (1967).
[6] M.-F. Luo, Z.-L. Yan, and L.-Y. Jin, J. Mol. Catal. A **260**, 157 (2006).
[7] H. He, H. X. Dai, and C. T. Au, Catal. Today **90**, 245 (2004).

[8]S. Rossignol, F. Gérard, D. Mesnard, C. Kappenstein, and D. Duprez, J. Mater. Chem. **13**, 3017 (2003).
[9]Z. Song, W. Liu, H. Nishiguchi, A. Takami, K. Nagaoka, and Y. Takita, Appl. Catal., A **329**, 86 (2007).
[10]C. T. Campbell, Surf. Sci. Rep. **27**, 1 (1997).
[11]C. R. Henry, Surf. Sci. Rep. **31**, 231 (1998).
[12]M. Bäumer and H.-J. Freund, Prog. Surf. Sci. **61**, 127 (1999).
[13]H. R. Huff and D. C. Gilmer, *High Dielectric Constant Materials* (Springer, Berlin, 2005).
[14]E. J. Tarsa, J. S. Speck, and Mc D. Robinson, Appl. Phys. Lett. **63**, 539 (1993).
[15]T. Schroeder, A. Giussani, J. Dabrowski, P. Zaumseil, H.-J. Müssig, O. Seifarth, and P. Storck, Phys. Status Solidi C **6**, 653 (2009).
[16]N. A. Elmasry, M. Hunter, A. Elnaggar, and S. M. Bedair, J. Appl. Phys. **98**, 106104 (2004).
[17]N. A. Bojarczuk, M. Copel, S. Guha, V. Narayanan, E. J. Preisler, F. M. Ross, and H. Shang, Appl. Phys. Lett. **83**, 5443 (2003).
[18]A. Giussani, O. Seifarth, P. Rodenbach, H.-J. Müssig, P. Zaumseil, T. Weisemöller, C. Deiter, J. Wollschläger, P. Storck, and T. Schroeder, J. Appl. Phys. **103**, 084110 (2008).
[19]C. Dubourdieu, I. Gelard, O. Salicio, G. Saint-Girons, B. Vilquin, and G. Holinger, Int. J. Nanotechnol. **7**, 320 (2010).
[20]R. Bachelet, P. de Coux, B. Warot-Fonrose, V. Skumryev, J. Fontcuberta, and F. Sánchez, Thin Solid Films **519**, 5726 (2011).
[21]H. Nagata, M. Yoshimoto, H. Koinuma, E. Min, and N. Haga, J. Cryst. Growth **123**, 1 (1992).
[22]T. Inoue, M. Osonoe, H. Tohda, M. Hiramatsu, Y. Yamamoto, A. Yamanaka, and T. Nakayama, J. Appl. Phys. **69**, 8313 (1991).
[23]S. Gevers, T. Weisemoeller, A. Schaefer, V. Zielasek, M. Bäumer, and J. Wollschläger, Phys. Rev. B **83**, 193408 (2011).
[24]A. Schaefer, V. Zielasek, T. Schmidt, A. Sandell, M. Schowalter, O. Seifarth, L. E. Walle, C. Schulz, J. Wollschläger, T. Schroeder, A. Rosenauer, J. Falta, and M. Bäumer, Phys. Rev. B **80**, 045414 (2009).
[25]T. Schroeder, P. Zaumseil, G. Weidner, J. Dabrowski, P. Storck, and H.-J. Müssig, J. Appl. Phys. **99**, 014101 (2006).
[26]Z. X. Mei, Y. Wang, X. L. Du, Z. Q. Zeng, M. J. Ying, H. Zheng, J. F. Jia, Q. K. Xue, and Z. Zhang, J. Cryst. Growth **289**, 686 (2006).
[27]N. Yu, P. C. McIntyre, M. Nastasi, and K. E. Sickafus, Phys. Rev. B **52**, 17518 (1995).
[28]T. Schroeder, P. Zaumseil, O. Seifarth, A. Giussani, H.-J. Müssig, P. Storck, D. Geiger, H. Lichte, and J. Dabrowski, New J. Phys. **10**, 113004 (2008).
[29]T. Schroeder, P. Zaumseil, G. Weidner, C. Wenger, G. Lupina, H.-J. Müssig, and P. Storck, J. Appl. Phys. **98**, 123513 (2005).
[30]A. Schaefer, T. Schroeder, G. Lupina, Y. Borchert, J. Dabrowski, C. Wenger, and M. Bäumer, Surf. Sci. **601**, 1473 (2007).
[31]J. P. Liu, P. Zaumseil, E. Bugiel, and H.-J. Osten, Appl. Phys. Lett. **79**, 671 (2001).
[32]P. Giannozzi *et al.*, J. Phys.: Condens. Matter **21**, 395502 (2009).
[33]J. P. Perdew and A. Zunger, Phys. Rev. B **23**, 5048 (1981).
[34]N. V. Skorodumova, M. Baudin, and K. Hermansson, Phys. Rev. B **69**, 075401 (2004).
[35]J. L. F. Da Silva, M. V. Ganduglia-Pirovano, J. Sauer, V. Bayer, and G. Kresse, Phys. Rev. B **75**, 045121 (2007).
[36]T. Weisemoeller, F. Bertram, S. Gevers, A. Greuling, C. Deiter, H. Tobergte, M. Neumann, J. Wollschläger, A. Giussani, and T. Schroeder, J. Appl. Phys. **105**, 124108 (2009).
[37]T. Schroeder, I. Costina, P. Storck, A. Wilke, O. Seifarth, A. Giussani, H. J. Müssig, and P. Zaumseil, J. Appl. Phys. **103**, 084102 (2008).
[38]T. Schroeder, I. Costina, A. Giussani, G. Weidner, O. Seifarth, C. Wenger, P. Zaumseil, C. Mocuta, T. H. Metzger, D. Geiger, and H. Lichte, J. Appl. Phys. **102**, 034107 (2007).
[39]R. M. Wallace and G. D. Wilk, Crit. Rev. Solid State Mater. Sci. **28**, 231 (2003).
[40]N. M. Jeutter, W. Moritz, A. Sidorenko, and A. Stierle, Appl. Phys. Lett. **90**, 062906 (2007).
[41]P. Zaumseil, J. Phys. D: Appl. Phys. **41**, 135308 (2008).
[42]P. Zaumseil and T. Schroeder, J. Phys. D: Appl. Phys. **44**, 055403 (2011).
[43]L. Eyring and N. C. Baenziger, J. Appl. Phys. **33**, 428 (1962).